

Bifurcation and multiple states in plane Couette flow with spanwise rotation

Xiang Yang¹ and Zhen-hua Xia²

¹ Mechanical Engineering, Pennsylvania State University, PA, USA, 16802

² Department of Engineering Mechanics, Zhejiang University, Hangzhou, China, 310027

Abstract

We present a derivation that begins with the Navier–Stokes equation and ends with a prediction of multiple statistically stable states identical to those observed in a spanwise rotating plane Couette flow. This derivation is able to explain the presence of multiple states in fully developed turbulence and the selection of one state over the other by differently sized computational domains and different initial conditions. According to the present derivation, two and only two statistically stable states are possible in an infinitely large plane Couette flow with spanwise rotation, and that multiple states are not possible at very slow or very rapid rotation speeds. We also show the existence of limit cycles near statistically stable states.

1 Introduction

According to the classical theory, turbulence is often thought to be ergodic when it is fully developed, that is, a turbulent flow visits all viable states in the phase space, leading to a unique statistical state, which is irrelevant to the initial conditions, at fixed control parameters (Frisch, 1995; Tsinober, 2001; Galanti and Tsinober, 2004). This ergodic assumption has profound influence on our thinking and how we approach a turbulent flow. For example, turbulence scalings, e.g., the logarithmic mean flow scaling redin wall-bounded turbulence (Marusic et al., 2013) and the $-5/3$ scaling of the energy spectrum, are defined assuming that the flow has one unique statistical state.

However, ergodicity of fully developed turbulence was challenged by multiple authors in the recent literature who observed multiple states in von Kármán flow (Ravelet et al., 2004, 2008), Rayleigh-Benard convection (Xi and Xia, 2008; Ahlers et al., 2011; van der Poel et al., 2011; Weiss and Ahlers, 2013; Xie et al., 2018), rotating Rayleigh-Bénard convection (Stevens et al., 2009; Weiss et al., 2010; Wei et al., 2015), Rayleigh-Bénard convection with tilted containers (Wang et al., 2018), Taylor-Couette flow (TCF) (Huisman et al., 2014; van der Veen et al., 2016; Gul et al., 2018), spherical-Couette flow (Zimmerman et al., 2011), Spanwise rotating plane Couette flow (RPCF) (Xia et al., 2018; Huang et al., 2019; Xia et al., 2019), forced rotating turbulence (Yokoyama and Takaoka, 2017) and double diffusive convection turbulence (Yang et al., 2020b). In some of the multistate cases, the state transition happens frequently at certain parameter range (Xi and Xia, 2008; Xie et al., 2018), while in other cases the different states are stable and robust, exhibiting hysteresis behavior when the control parameter varies (Huisman et al., 2014; Yokoyama and Takaoka, 2017; Huang et al., 2019; Yang et al., 2020b). Huisman et al. (2014) showed that different phase-space trajectories could lead to different torques and velocity distributions at the same flow condition in a TCF at a Reynolds number $Re \sim 10^6$, suggesting the presence of two possible turbulent states in a laboratory context. The multiple states in TCF was also reported by van der Veen et al. (2016) who observed multiple states in two experimental setups with different aspect ratios for the working Taylor numbers covering almost two decades, inferring that multiple states in highly turbulent TCF are very robust and they may be expected

to persist when $Ta \geq 10^{13}$. [Huang et al. \(2019\)](#) reported the hysteresis behavior in RPCF based on two groups of direct numerical simulations at $Re_w = 1300$ (see the definition below) with the rotation number Ro varying sequentially in steps in two opposite directions, which is mimicking the experimental setups in [Huisman et al. \(2014\)](#). With fixed streamwise and spanwise lengths of computational domain, $8\pi h$ and $4\pi h$, the flow prefers a state with two pairs of roll cells when Ro increases from 0.02 to 0.5 while it prefers the state with three pairs of roll cells when Ro decreases from 0.5 to 0.02. The flow structures and turbulent statistics also lead to the hysteresis loops.

These observations have brought many interesting discussions, nonetheless, the research on this topic is, by and large, phenomenological. That is, conclusions were drawn from data with very little or no idea whether they could be applied to a different flow. In [Huisman et al. \(2014\)](#), they conjectured that the selectability of the large-scale coherent structures plays a very important role in the multiple states of TCF. [van der Veen et al. \(2016\)](#) also mentioned that a theoretical understanding of the values of rotation rate at which the systems transits between states remains elusive. Although [Xia et al. \(2019\)](#) showed the large-scale roll cells at different flow states indeed play an important role through detailed turbulent statistics in RPCF, they have not answered the origin of the two states, and many related questions remain open. Here, we name a few. First, it is not clearly whether multiple states exist at all rotation speeds. Second, it is not known if there could be more than two statistically stable states at a given flow condition. Other unexplained observations include the selection of one state over the other by differently sized computational domains and the selection of the states by initial conditions ([Xia et al., 2019](#)). In all, a theoretical analysis is in need to help to interpret the experimental and computational observations. The objective of this work is to fill in this gap as much as we can.

Before proceeding with our derivation, we briefly review the previous theoretical works. From a fundamental standpoint, many of the ideas in the following sections are similar to these expressed in the field of statistical state dynamics (SSD) ([Farrell and Ioannou, 2007, 2014](#)) and the related fields of research ([Taira et al., 2017; Farrell et al., 2017](#)). In particular, SSD recognizes that the dynamics of turbulent statistical state is time dependent, in which case the statistics obtained from many realizations would not in general correspond to a representation of the statistical state at any time. While this implies “multiple” states, SSD typically follows Kolmogorov and assumes ergodicity, i.e., the statistical average of a turbulent system asymptotically approach a fixed point. Operationally, we will apply truncated Galerkin projection (TGP) of the Navier–Stokes (NS) equation to a pre-defined sub-space. TGP sees most use in dynamical systems ([Majda and Timofeyev, 2000; Rapún and Vega, 2010](#)). A recent application of this methodology in turbulence research could be found [Anderson \(2019\)](#), which led to non-periodic phase-space trajectories of roughness-driven secondary flows in high Reynolds number boundary layers.

The rest of the paper is organized as follows. A more in-depth summary of the multiple states phenomenology in spanwise rotating plane Couette flow is presented in section 2. We will use this data to anchor our derivation. We present our derivation in sections 3. The results are presented in section 4, followed by conclusions in section 5. We try to keep the derivation simple and analytically tractable. To that end, discussion that involves numerical tools and tediously long algebra are moved to the appendices.

2 Multiple states phenomenology in plane Couette flow

In this section, we present a more in-depth summary of the multiple states phenomenology in plane Couette flow. Again, we will use these data to anchor our theoretical derivation. [Xia et al. \(2018\)](#)

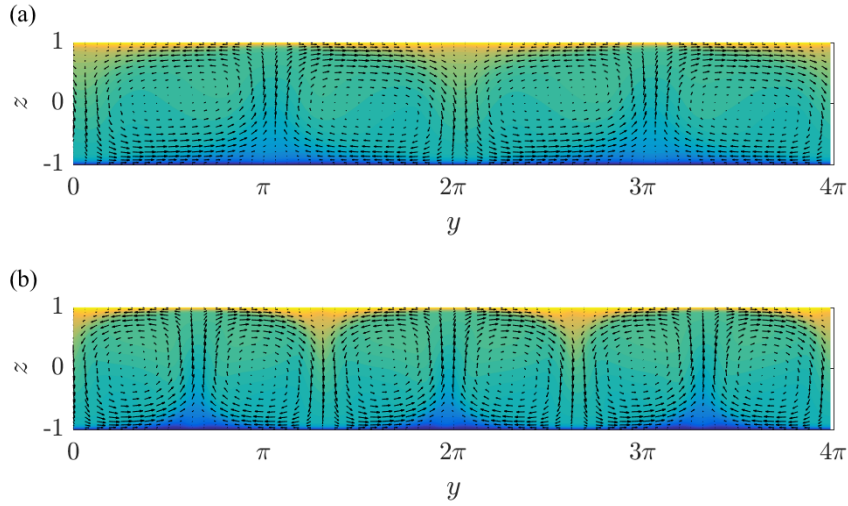


Figure 1: (a) Contours of the time and streamwise averaged streamwise velocity. The velocity shows the in-plane motion. This statistically stable state features two pairs of roll cells. (b) Same as (a) but for a state that features three pairs of roll cells. Here, yellow represents high streamwise velocity, blue represents low velocity, and green is in between. The exact values are not important here.

reported two statistically stable states in spanwise rotating channel at $Re_w = U_w h / \nu = 1300$ and $Ro = 2\Omega h / U_w = 0.2$. It may be worth mentioning that the coordinate system in [Xia et al. \(2018\)](#) is different from the one here. Per the coordinate system here, the spanwise rotation is in the $-y$ direction. The two states feature two and three pairs of roll cells in a periodic domain of size $L_x \times L_y \times L_z = 10\pi h \times 4\pi h \times 2h$, as shown in figure 1. Here, h is the half channel height, U_w is half of the velocity difference between two plates, Ω is the angular velocity in the spanwise direction, ν is the kinematic viscosity, x , y , and z denote the streamwise, spanwise, and wall-normal directions, L_x , L_y , and L_z are the domain sizes in the x , y , and z directions. Throughout the paper, the two states with two pairs and three pairs of roll cells will be referred to as R2 and R3 respectively.

The data in [Xia et al. \(2018\)](#) suggests that the roll cells in both R2 and R3 are nearly streamwise homogeneous. This observation will lead to one of the simplifications in the next section. Moreover, while R2 and R3 lead to disparate dispersive stresses, the mean flows in R2 and R3 are very similar, see figure 2. In a follow-up work, [Huang et al. \(2019\)](#) found that the flow is more likely to converge to R2 when increasing the rotation speed from $Ro = 0.02$ to $Ro = 0.5$ and the flow is more likely to converge to R3 when decreasing the rotation speed from $Ro = 0.5$ to $Ro = 0.02$. In another follow-up work, [Xia et al. \(2019\)](#) synthesized a few initial conditions by linearly interpolating between R2 and R3 and reported that the flow is more likely to converge to R2 if the interpolation is biased towards R2 and vice versa. Furthermore, they showed that the energy transfer from the mean field to the secondary and residual fields are different at the two states, where most of the kinetic energy is transferred to the residual fields through the streamwise secondary flows in R3 state while the transfer directly from the mean field through the production term dominates over other terms in R2 state.

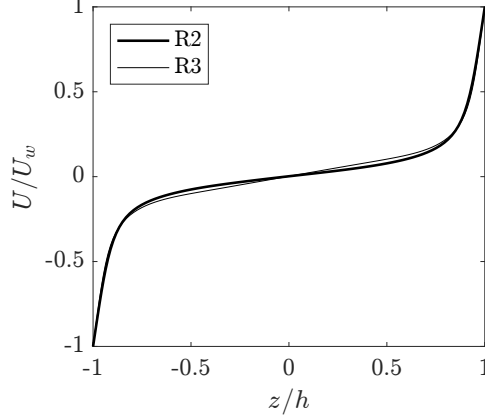


Figure 2: Horizontally and time averaged streamwise velocity. Normalization is by U_w and h .

3 Roll cell dynamics

The multiple states in plane Couette flow concern with the dynamics of the roll cells. In this section, we will extract from the NS equation two equations that govern the the dynamics of the roll cells.

3.1 Theoretical derivation

Turbulence has many degrees of freedom, which gives rise to a high dimensional phase space. Directly studying turbulent dynamics in a high dimensional phase space is difficult (if not impossible). In order to make progress, we must simplify the NS equation according to the specific flow under consideration.

The NS equation for RPCF reads

$$\frac{Du_i}{Dt} = -\frac{1}{\rho} \frac{\partial p}{\partial x_i} + \nu \frac{\partial^2 u_i}{\partial x_k^2} - \epsilon_{i2k} Ro u_k, \quad (1)$$

where u_i is the fluid velocity in the i th Cartesian direction, D/Dt is the total derivative, $i = 1, 2, 3$ denote the the streamwise, spanwise, and wall-normal directions. We use x, y, z interchangeably with x_i ; u, v, w interchangeably with u_i ; and ∂_i interchangeably with $\partial/\partial x_i$. Normalization is by the half of the wall velocity difference U_w , and the half channel height h . It follows that $\nu = 1/Re_w$, where $Re_w = U_w h/\nu$ is the Reynolds number. In the main text, we present derivations for plane Couette flow. Derivations for Taylor Couette flow (which concerns with surface curvature) are presented in appendix A.

First, we filter the NS equation in the streamwise direction at a scale $\sim O(h)$. The filtered streamwise velocity equation reads

$$\frac{D\tilde{u}_1}{Dt} = -\frac{1}{\rho} \partial_1 \tilde{p} - \partial_j \tilde{T}_{1j} + \nu \partial_j \partial_j \tilde{u}_1 - Ro \tilde{u}_3, \quad (2)$$

where $\tilde{\cdot}$ denotes streamwise filtration, and \tilde{T}_{1j} is the turbulent stress. Define the filtered vorticity

$\tilde{\omega}_i = \epsilon_{ijk} \partial_j \tilde{u}_k$. The streamwise vorticity equation reads

$$\frac{D\tilde{\omega}_1}{Dt} = \tilde{\omega}_j \partial_j \tilde{u}_1 - \epsilon_{1qi} \partial_q \partial_j \tilde{T}_{ij} + \nu \partial_j \partial_j \tilde{\omega}_1 + Ro \partial_2 \tilde{u}_1. \quad (3)$$

For a spanwise rotating plane Couette flow that features multiple statistically stable states, the flow is approximately streamwise homogeneous. To focus on the behavior of the large-scale roll cells, we neglect the streamwise derivative and invoke the eddy viscosity model. It follows that the vortex stretching term $\tilde{\omega}_j \partial_j \tilde{u}_1$ is zero upon substitution of the vorticity, $\tilde{\omega}_j = \epsilon_{j pq} \partial_p \tilde{u}_q$. Hence, (2) and (3) lead to

$$\partial_t \tilde{u}_1 + \tilde{u}_j \partial_j \tilde{u}_1 = \partial_j [(\nu + \nu_t) \partial_j \tilde{u}_1] - Ro \tilde{u}_3, \quad (4)$$

and

$$\partial_t \tilde{\omega}_1 + \tilde{u}_j \partial_j \tilde{\omega}_1 = \partial_j [(\nu + \nu_t) \partial_j \tilde{\omega}_1] + Ro \partial_2 \tilde{u}_1, \quad (5)$$

where $j = 2, 3$ with Einstein summation, and $\partial_{jj} = \partial_{22} + \partial_{33}$.

Second, we define a streamfunction ψ such that

$$\begin{aligned} \tilde{u}_2 &= \partial_3 \psi, \\ \tilde{u}_3 &= -\partial_2 \psi. \end{aligned} \quad (6)$$

It follows that $\tilde{\omega}_1 = -\partial_j \partial_j \psi$. Plugging (6) into (4) and (5) leads to

$$\partial_t \tilde{u}_1 + \partial_2 \tilde{u}_1 \partial_3 \psi - \partial_3 \tilde{u}_1 \partial_2 \psi = \partial_j \left[\frac{1}{R} \partial_j \tilde{u}_1 \right] + Ro \partial_2 \psi \quad (7)$$

and

$$\partial_t \partial_j \partial_j \psi + \partial_2 \partial_j \partial_j \psi \partial_3 \psi - \partial_3 \partial_j \partial_j \psi \partial_2 \psi = \partial_j \left[\frac{1}{R} \partial_j \partial_q \partial_q \psi \right] - Ro \partial_2 \tilde{u}_1. \quad (8)$$

In the above equation, we have invoked the effective Reynolds number $R = 1/(\nu + \nu_t)$ following, e.g., [Anderson \(2019\)](#). As the eddy viscosity is usually not a constant, invoking the effective Reynolds number is to resort to an approximation that works. Nonetheless, in this context, because the eddy viscosity in the bulk region of a spanwise rotating channel is in fact close to a constant ([Yang et al., 2020a](#)), invoking the effective Reynolds number here has a somewhat sounder physical basis.

Third, we project (7) and (8) on a statistically stable state

$$\begin{aligned} \psi(x_2, x_3, t) &= a(t) \alpha(x_2, x_3), \\ \tilde{u}_1(x_2, x_3, t) &= b(t) \beta(x_2, x_3) + U(x_3), \end{aligned} \quad (9)$$

where α and β represent roll cells of a given wavenumber, and $U(x_3)$ is the mean flow. Here, we assume that the mean flow does not depend on a particular state. This assumption is consistent with the data and simplifies the analysis that follows. Relaxing this assumption leads to more involved math but essentially the same conclusions, as shown in [Appendix B](#). Plugging (9) into (7) and (8)

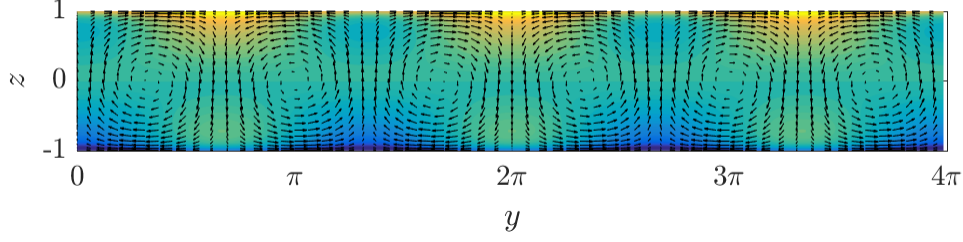


Figure 3: Equation (12). Contours are for u and vectors are for v and w . Again, the exact contour values are not important.

leads to

$$\begin{aligned} & \beta \frac{db}{dt} + ab\partial_2\beta\partial_3\alpha - ab\partial_3\beta\partial_2\alpha - a\partial_3U\partial_2\alpha \\ &= \frac{1}{R} b\partial_j\partial_j\beta + \frac{1}{R}\partial_3\partial_3U + Ro a\partial_2\alpha \end{aligned} \quad (10)$$

and

$$\begin{aligned} & \partial_j\partial_j\alpha \frac{da}{dt} + a^2(\partial_2\partial_j\partial_j\alpha\partial_3\alpha - \partial_3\partial_j\partial_j\alpha\partial_2\alpha) \\ &= \frac{1}{R} a [\partial_2^4\alpha + 2\partial_2^2\partial_3^2\alpha + \partial_3^4\alpha] - Ro b\partial_2\beta \end{aligned} \quad (11)$$

Equations (10) and (11) govern the dynamics of roll cells. In (10) and (11), we have left the α and β as generic functions of y and z , and, importantly, we have retained non-linearity.

Fourth, we need ansatzes for α and β in order to advance. The DNS solution is by itself a good ansatz, but the use of DNS data necessarily involves numerical tools in the following derivations, which will be postponed to Appendix C. Here, we use the following analytical ansatz to approximate the multiple states

$$\begin{aligned} \alpha &= -\sin\left(\frac{\pi}{2}ky\right)\cos\left(\frac{\pi}{2}z\right), \\ \beta &= -\cos\left(\frac{\pi}{2}ky\right)[1 - \cos(\pi z)]. \end{aligned} \quad (12)$$

Figure 3 shows the ansatz for $k = 3/\pi$, which corresponds to R3. As we can see, the ansatz compares well with the data, i.e., figure 1 (b). Quantitatively, our analytical ansatz contains about 55% of the energy in \tilde{u} and about 90% of the energy in \tilde{v} and \tilde{w} . The next most energetic Fourier mode contains about 7% of the energy in \tilde{u} and 1% of the energy in \tilde{v} and \tilde{w} . For R2, our analytical ansatz contains about 60% of the energy in \tilde{u} and about 85% of the energy in \tilde{v} and \tilde{w} . The next most energetic Fourier mode contains about 7% of the energy in \tilde{u} and about 4% of the energy in \tilde{v} and \tilde{w} . One could obtain more realistic ansatzes by including additional terms in (12). Figure 4 shows the energy contained in the ansatzes as we include more Fourier modes. As one would expect, accuracy comes at the price of brevity. In appendix C, we resort to DNS for an ansatz, and we will see that our conclusions are not affected.

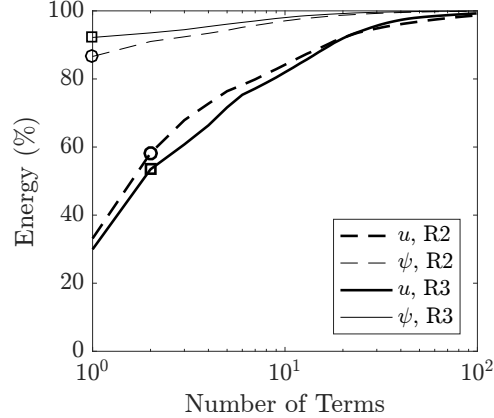


Figure 4: The energy contained in the ansatz as a function of n , where n is the number of terms in the ansatz. The thick lines are for u . The thin lines are for ψ . The dashed lines are for R2. The solid lines are for R3.

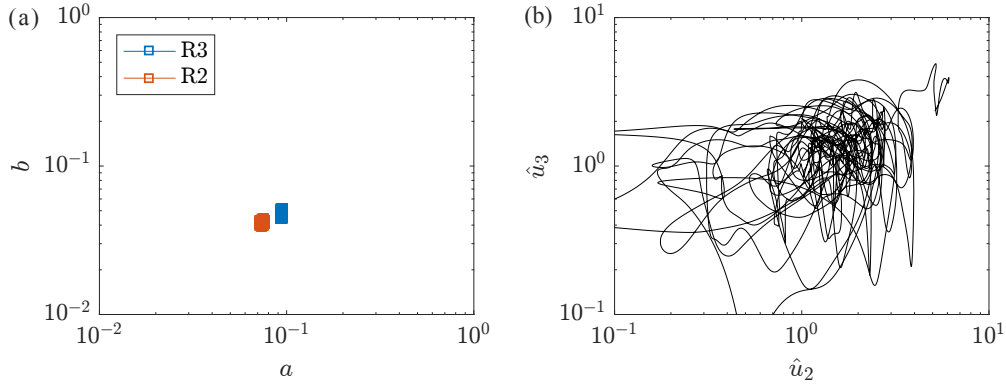


Figure 5: (a) Trajectories of R2 and R3 in the phase space of a and b . (b) Trajectory of isotropic turbulence in the sub-phase space of two Fourier modes \hat{u}_2 and \hat{u}_3 . The x and y axes in both figures span two decades.

3.2 Dynamics of the stable states

Before we proceed with our derivation, we take a closer look at the flow dynamics near the two stable states in R2 and R3 so that we have in mind what to expect. Equations (10) and (11) map the roll cell dynamics to two modes: a and b . Projecting the DNS data on the ansatzes in (12), in figures 5 (a), we plot the trajectories of R2 and R3 in the phase space of a and b . For comparison, in figure 5 (b), we plot the trajectory of an isotropic flow in the sub-phase-space of two Fourier modes. The integral length of this isotropic flow is L . The two Fourier modes correspond to the length scales of $L/2$ and $L/8$ (relatively large scale modes). Details of the data in figure 5 (b) are presented in Appendix D.

Comparing figures 5 (a, b), the trajectory in figure 5 (b) visits a large area in the phase space and is easily ergodic, but the two trajectories in figure 5 (a) are confined in two small regions, and the two regions do not overlap, thereby leading to two independent statistically stable states.

Figures 6 (a, b) show a zoom-in view of the trajectories of R2 and R3 respectively in the phase space of a' and b' , where the superscript \prime denotes temporal fluctuations. Limit-cycle like

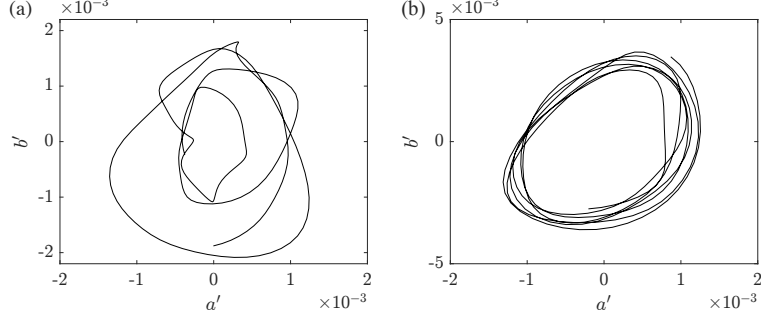


Figure 6: Zoomed view of the trajectories of (a) R2 and (b) R3 in the phase space of a' and b' .

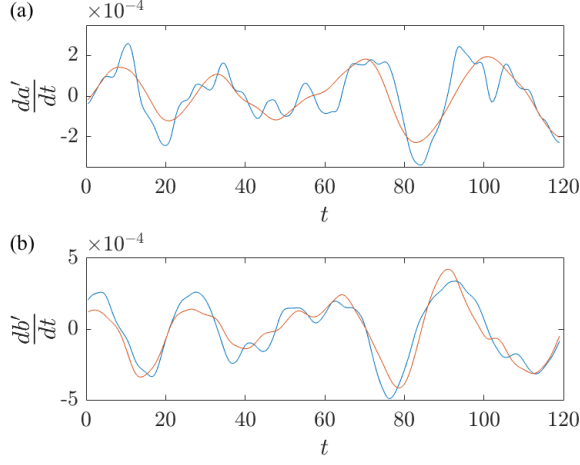


Figure 7: The time evolution of (a) a' and (b) b' in R2 and fits to linear dynamics.

trajectories are found in both R2 and R3. For reasons that will be clear in the next subsection, we fit da'/dt and db'/dt to the linear dynamics, i.e., $c_1 a' + c_2 b'$, where c_1, c_2 are constants. In figures 7 and 8, the data is compared to the linear dynamics, and the two are remarkably similar, suggesting that the flow near the two stable states is govern by linear dynamics. Ergodicity relies on sufficiently large fluctuations, and in a turbulent flow system, large fluctuations are often results of non-linear interactions. The fact that the evolution of a' and b' follows linear dynamics explains, from a phenomenological standpoint, why the flow is trapped within a stable state. The challenge remains that whether we could theoretical show that a and b follow linear dynamics from the NS equation.

3.3 Truncated Galerkin projection and bifurcation analysis

We will proceed with our derivation. In section 3.1, we were at step four. In section 3.2, we see that the data suggests linear dynamics near a stable state. In this section, we will see if our derivation gives rise to the observed linear dynamics. The fifth step is to plug (12) into (10) and (11) and project the two equations on to the ansatzes in (12). Here, projecting a function f on α is to integrate

$$\int_0^{L_y} \int_{-1}^1 f \cdot \alpha dz dy. \quad (13)$$

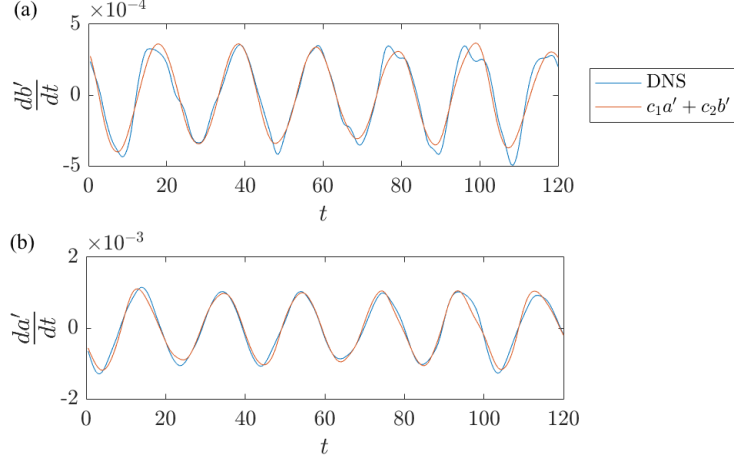


Figure 8: The time evolution of (a) a' and (b) b' in R3 and fits to linear dynamics.

After some (long) algebra, we arrive at

$$\frac{db}{dt} = \left[\frac{4k}{9} Ro + \frac{k\pi}{3} \int_{-1}^1 \sin^2\left(\frac{\pi}{2}z\right) \cos\left(\frac{\pi}{2}z\right) \frac{dU}{dz} dz \right] a - \left(k^2 + \frac{4}{3} \right) \frac{1}{R} \left(\frac{\pi}{2} \right)^2 b \quad (14)$$

and

$$\frac{da}{dt} = -\frac{1}{R} (k^2 + 1) (\pi/2)^2 a - \frac{4}{3} \frac{k}{k^2 + 1} Ro (\pi/2)^{-2} b, \quad (15)$$

which is linear dynamics. In arriving at the above two equations, we invoke $\sin(\pi/2 k L_y) = 0$ since there can only be integer pairs of roll cells in the domain. It is worth noting that truncated Galerkin projection does not preclude nonlinearity. For instance, [Anderson \(2019\)](#) obtained a truncated system with nonlinear terms. The integral in (14) is

$$\int_{-1}^1 \sin^2\left(\frac{\pi}{2}z\right) \cos\left(\frac{\pi}{2}z\right) \frac{dU}{dz} dz = - \int_{-1}^1 U \frac{\pi}{2} \sin\left(\frac{\pi}{2}z\right) \left[2 - 3 \sin^2\left(\frac{\pi}{2}z\right) \right] dz \approx 0.27 \quad (16)$$

for both R2 and R3. As is clear from (16), the integral concerns with U not its derivative.

We are now at the last step. Sixth, we conduct bifurcation analysis of the ODEs in (14) and (15). If multiple statistically stable state exist, $da/dt = 0$ and $db/dt = 0$ must have multiple non-trivial solutions. Hence, if multiple states exist, the eigen values of the ODEs in (14) and (15) must be such that

$$\lambda_{1,2} = 0, \quad (17)$$

for non-trivial a and b . This necessarily leads to:

$$(k^2 + 1)^2 (k^2 + 4/3) - C k^2 = 0, \quad C \approx - (0.039 Ro^2 + 0.025 Ro) R^2 \quad (18)$$

Equation (18) is a cubic equation of k^2 (note that $Ro < 0$ and $C > 0$). For certain C , i.e., for certain flow condition, there are two physically viable roots:

$$\begin{aligned} k_1^2 &= h^{1/3} + gh^{-1/3} - 10/9, \\ k_2^2 &= -i\sqrt{3/4} \times (h^{1/3} - gh^{-1/3}) - 1/2 \times (h^{1/3} + gh^{-1/3}) - 10/9, \end{aligned} \quad (19)$$

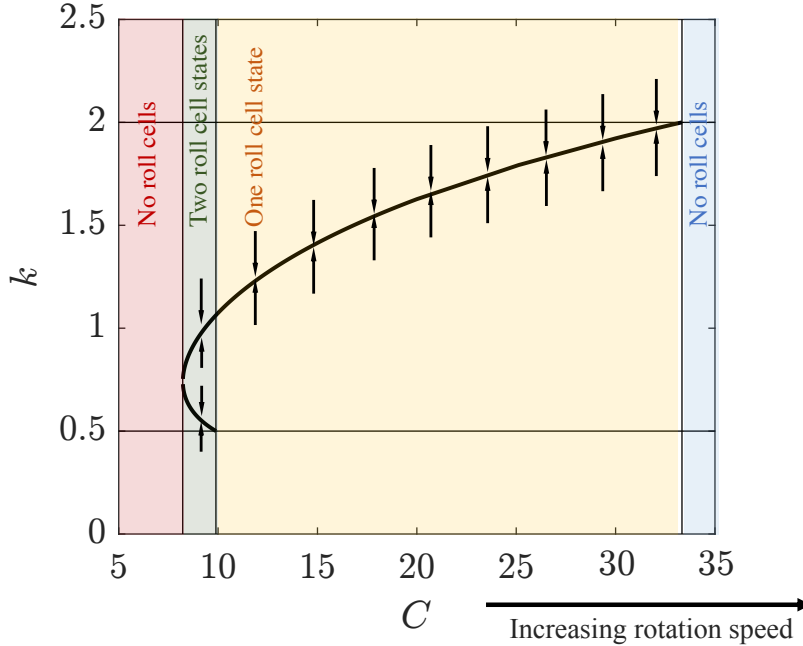


Figure 9: Bifurcation diagram. Per (18), $C \approx -(0.039Ro^2 + 0.025Ro)R^2$. For the condition considered here, i.e., near $Ro = -0.2$, C is an increasing function of the rotation speed $|Ro|$.

where $f = 5C/9 + 1/729$, $g = C/3 + 1/81$, $h = (f^2 - g^3)^{1/2} - f$, $i = \sqrt{-1}$, $i^{1/3} = \exp(i \cdot \pi/6)$, $(-i)^{1/3} = \exp(-i \cdot \pi/6)$. Here, k_2^2 is real and is positive despite the appearance of the unit imaginary number i . Hydrodynamic stability does not allow for very slim nor very fat roll cells (Drazin and Reid, 2004). Determining the limits of roll cells' aspect ratio falls out of the scope of this paper. Here, we arbitrarily cutoff at $k = 0.5$ and $k = 2$, constraining that the roll cells' heights to be no more than twice of their widths and no less than half of their widths. Figure 9 shows the bifurcation diagram, where we plot k_1 and k_2 as a function of C . We concludes our derivation here.

Before we proceed with predictions, we make two observations. First, truncated Galerkin projection is known to preserve non-linearity in the equation, however, the application of truncated Galerkin projection to this particular problem has led to linear dynamics. Second, (18) is, strictly speaking, a sextic polynomial, which, in principle, has 6 roots. Nonetheless, it turns out that if one regards k^2 as the unknown, the equation reduces to a cubic one; and it also happens that one of the three roots of the cubic equation is always negative, leaving us only two physically viable roots.

4 Predictions of the theory

4.1 multiple states in an infinitely large domain

Per figure 9, for small values of Ro , the flow is in the red zone and there are no physically viable root to Eq. (18). It follows that, for a non-rotating plane Couette flow, multiple states that feature roll cells with different wavenumbers are not possible. For a flow that is in the green zone, i.e., for a moderate rotation number, (18) has two roots between 0.5 and 2, leading to multiple states. In the yellow zone, i.e., at high rotation speeds, (18) has one root between 0.5 and 2. This means that while roll cells could still be found, they could only be found at one wavenumber. In the blue

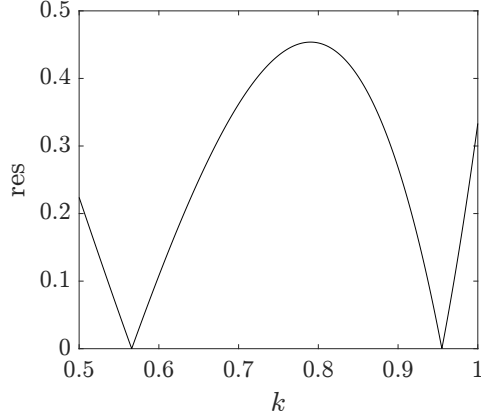


Figure 10: Residual of (18) for $C = 9$.

zone, i.e., at very high rotation speeds, (18) does not have a root between 0.5 and 2, and no roll cells could be found. For a C that gives rise to multiple states, e.g., $C = 9$, we plot the residual of the cubic equation (18) in figure 10. The two statistically stable states yields 0. The residual measures the distance of a state from the equilibrium and therefore can be interpreted as a measure of the energy level. From figure 10, we see that the large energy barrier between the stable states locks the flow at one state, leading to non-ergodicity. The system would have been ergodic if the energy barrier is low or if the flow has enough energy to go from one state to the other.

4.2 multiple states in a finite domain

Finite domain admits only a few discrete wavenumbers. For a domain that extends about $L_y = 4\pi$ in the spanwise direction, the wavenumber k can only take values $1/\pi, 2/\pi, 3/\pi, \dots$, as sketched in figure 11 (a). According to figure 11 (a), for a $L_y = 4\pi$ domain, $k = 2/\pi$ and $k = 3/\pi$ are two possible statistically stable states. Had the domain size been $L_y = 2\pi$, no multiple states would be possible, as shown figure 11 (b). This explains the selection of certain state by domain. Last, observe the slight imbalance between $k = 2/\pi$ and $k = 3/\pi$. This imbalance makes R2 the preferred state if one increases the rotation speed from 0 to $Ro=0.2$ (i.e., C increases from 0) and R3 the preferred state if one decreases the rotation speed from 0.5 to 0.2 (i.e., C decreases from a large number), thereby explaining the selection of one state over the other by the initial condition (Huang et al., 2019). Allowing for some imbalance, the bifurcation diagram would in fact allow for three and four multiple states in a finite domain, as sketched in figure 11 (c).

5 Conclusions

We present an analytically tractable derivation that gives rise to multiple states in rotating flows. We show that non-ergodicity in a spanwise rotating channel is because the flow does not have the energy to escape a statistically stable state. According to this derivation, spanwise rotating plane Couette flow in an infinitely large domain can have two and only two statistically stable states. Finite domains (albeit with periodic boundary conditions in the horizontal directions) admit wavenumbers at a few discrete values. This gives rise to the observed selection of certain statistically stable state by differently sized domain and different initial conditions. A few straightforward extensions of our theory are presented in the appendices. They either involve the use of numerical tools, which enable us to handle more degrees of freedom, or long math derivations.

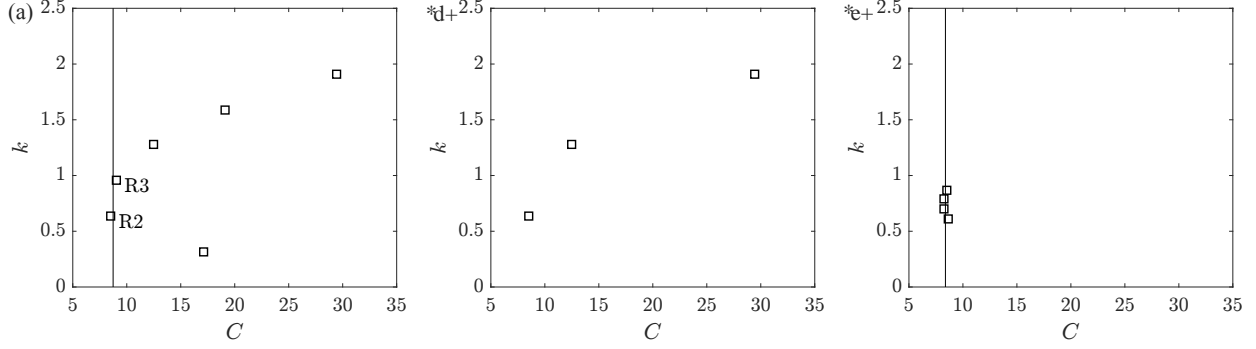


Figure 11: (a) Bifurcation diagram for a $L_y = 4\pi$ domain. The wavenumber only takes value at $k = n/\pi$. (b) Bifurcation diagram for a $L_y = 2\pi$ domain. The wavenumber only takes value at $2n/\pi$. (c) Bifurcation diagram for a finite domain. The four wavenumbers are equally distanced from the equilibrium.

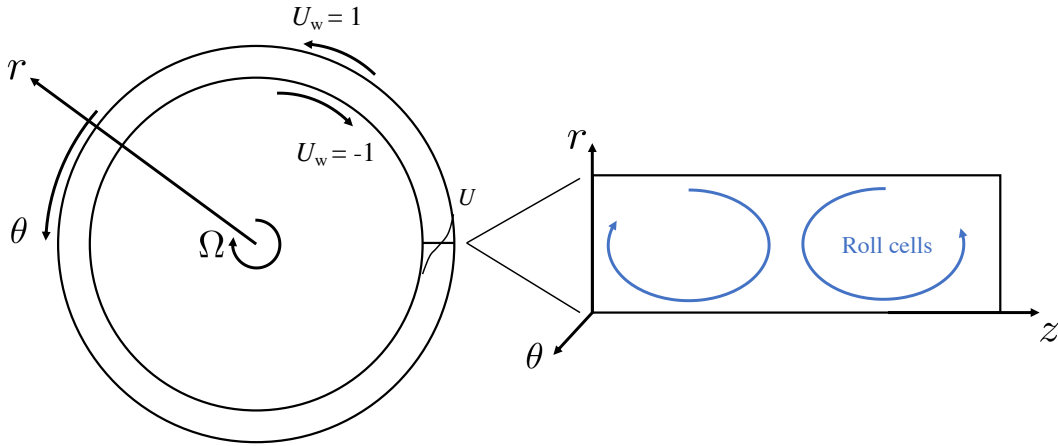


Figure 12: A sketch of Taylor-Couette flow.

Refining this derivation to a point where it could make more quantitative predictions, like the exact rotation number from which we can observe multiple states, is tantalizingly out of reach at this moment and will be the focus of the future research.

Acknowledgement

Yang hopes to thank Charle Meneveau, John Cimbala and Rob Kunz for useful inputs. Yang acknowledges ONR for financial support. Xia acknowledges the support from NSFC (Grant Nos. 11822208 and 11772297)

Appendix

A Taylor-Couette flow

Figure 12 is a sketch of Taylor Couette flow. θ is the “streamwise” direction, z is the “spanwise” direction, and r is the “wall-normal” direction. Without loss of generality, the radius of the outer cylinder is $r = r_0 + 1$ and the radius of the inner cylinder is $r = r_0 - 1$. The azimuthal filtered

flow is approximately homogeneous in the θ direction. Repeat the first step but for Taylor-Couette flow, we get two equations that governs the dynamics of \tilde{u}_θ and $\tilde{\omega}_\theta$:

$$\begin{aligned}\frac{\partial \tilde{u}_\theta}{\partial t} + \tilde{u}_r \frac{\partial \tilde{u}_\theta}{\partial r} + \frac{\tilde{u}_r \tilde{u}_\theta}{r} + \tilde{u}_z \frac{\partial \tilde{u}_\theta}{\partial z} &= \frac{1}{R} \left[\frac{1}{r} \frac{\partial}{\partial r} \left(r \frac{\partial \tilde{u}_\theta}{\partial r} \right) - \frac{\tilde{u}_\theta}{r^2} + \frac{\partial^2 \tilde{u}_\theta}{\partial z^2} \right] - Ro \tilde{u}_r \\ \frac{\partial \tilde{\omega}_\theta}{\partial t} + \tilde{u}_r \frac{\partial \tilde{\omega}_\theta}{\partial r} + \tilde{u}_z \frac{\partial \tilde{\omega}_\theta}{\partial z} &= \frac{1}{R} \left[\frac{\partial^2 \tilde{\omega}_\theta}{\partial r^2} + \frac{1}{r} \frac{\partial \tilde{\omega}_\theta}{\partial r} + \frac{\partial^2 \tilde{\omega}_\theta}{\partial z^2} \right] + Ro \frac{\partial \tilde{u}_\theta}{\partial z}.\end{aligned}\quad (20)$$

Observe that for $r_0 \gg 1$, (20) reduces to (4) and (5) (upon a coordinate transformation that maps θ to x , z to y , and r to z). A streamline function ψ could be defined:

$$\begin{aligned}\tilde{u}_r &= -\frac{1}{r} \frac{\partial \psi}{\partial z}, \\ \tilde{u}_z &= \frac{1}{r} \frac{\partial \psi}{\partial r},\end{aligned}\quad (21)$$

and it follows that the vorticity in the ω direction is

$$\tilde{\omega}_\theta = -\frac{1}{r} \left[\frac{\partial^2 \psi}{\partial z^2} + \frac{\partial^2 \psi}{\partial r^2} - \frac{1}{r} \frac{\partial \psi}{\partial r} \right].\quad (22)$$

Repeating step two and plugging (21) and (22) into (20) lead to two equations for \tilde{u}_θ and ψ , similar to (7) and (8).

Further advancements will require ansatzes for the roll cells. Without loss of generality, a possible ansatz is

$$\begin{aligned}\psi &= a(t)\alpha(r, z), \quad \alpha(r, z) = -r_0 \sin\left(\frac{\pi}{2}kz\right) \cos\left(\frac{\pi}{2}r\right); \\ \tilde{u}_\theta &= b(t)\beta(r, z), \quad \beta(r, z) = -\cos\left(\frac{\pi}{2}kz\right) (1 - \cos(\pi r)).\end{aligned}\quad (23)$$

Proceeding with steps five will lead to two ODEs for $a(t)$ and $b(t)$, whose non-trivial nodes give the statistically stable states. However, such analysis involves integrals that could not be evaluated analytically. Also, considering that we do not have access to the Taylor-Couette flow data, we will not pursue this analysis in this paper.

B Account for interactions between the mean flow and the roll cells

We add an additional term $c(t)\gamma(x_3)$ to the ansatz of \tilde{u}_1 in order to model the interactions between the mean flow and the roll cells:

$$\begin{aligned}\psi(x_2, x_3, t) &= a(t)\alpha(x_2, x_3), \\ \tilde{u}_1(x_2, x_3, t) &= b(t)\beta(x_2, x_3) + c(t)\gamma(x_3) + U(x_3).\end{aligned}\quad (24)$$

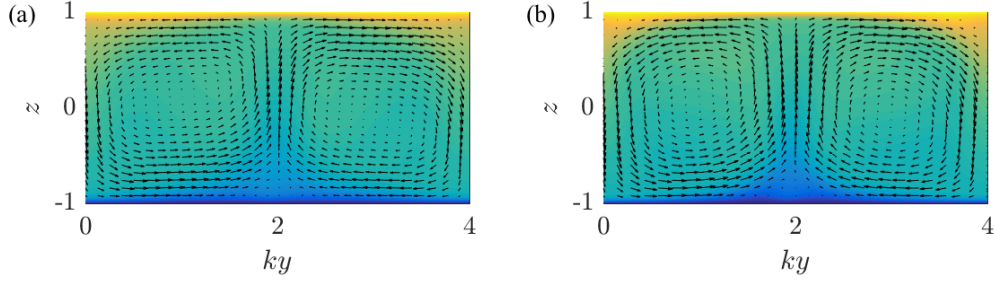


Figure 13: (a) A roll cell in R2. (b) A roll cell in R3. Legends are the same as in figure 1. The y axis is scaled such that ky is from 0 to 4. Again, the exact value of the contour is not relevant.

Repeating step three and plugging (24) into (7) lead to

$$\begin{aligned} & \beta \frac{db}{dt} + \gamma \frac{dc}{dt} + ab\partial_2\beta\partial_3\alpha - ab\partial_3\beta\partial_2\alpha - a\partial_3U\partial_2\alpha - ac\partial_3\gamma\partial_2\alpha \\ & = \frac{b}{R}\partial_j\partial_j\beta + \frac{1}{R}\partial_3\partial_3U + \frac{c}{R}\partial_3\partial_3\gamma + Ro a\partial_2\alpha, \end{aligned} \quad (25)$$

and plugging (24) into (8) leads to (11). Next, we repeat step four by using the same ansatz in (12) for α and β . The following ansatz for γ

$$\gamma = -\sin(\pi z). \quad (26)$$

Repeating step 5 and projecting (25) onto β and γ leads to

$$\begin{aligned} \frac{db}{dt} &= \left[\frac{4k}{9}Ro + \frac{0.14\pi k}{3} \right] a - \left(k^2 + \frac{4}{3} \right) \frac{1}{R} \left(\frac{\pi}{2} \right)^2 b + \frac{4\pi k}{45}ac, \\ \frac{dc}{dt} &= -\frac{\pi^2}{R}c - \frac{2\pi k}{15}ab. \end{aligned} \quad (27)$$

Projecting (11) onto α leads to (15). Equations (27) and (15) govern the roll cell dynamics. The ODEs in (27) and (15), however, have the same non-trivial node as (14) and (15) with $c = 0$.

C Data-based ansatz for roll cells

The DNS solution gives a good ansatz for the roll cells. Figures 13 (a, b) show the re-scaled roll cells in R2 and R3, and they are very similar. The following calculation will use the roll-cell solution in R2.

The velocities u, v, w in R2 are related to the ansatz as follows

$$u \sim \beta, \quad v \sim \partial_z\alpha, \quad w \sim -(2/\pi)\partial_{ky}\alpha. \quad (28)$$

Repeating step five and plugging α and β into (10) and (11) and projecting (10) and (11) on α

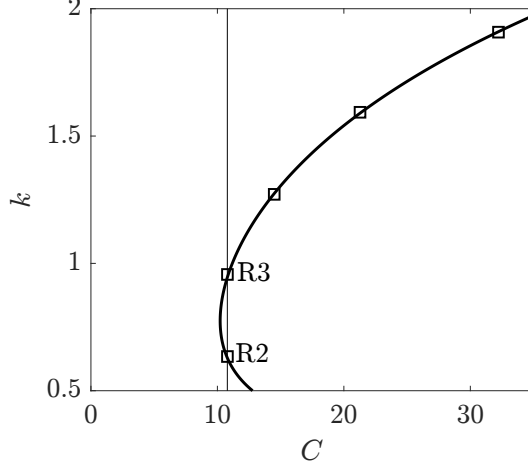


Figure 14: Bifurcation diagram of the system in (29).

and β , we have

$$\begin{aligned} \frac{db}{dt} &= (0.15 + 0.85 Ro)k a - (7.4k^2 + 14)\frac{b}{R} \\ \frac{da}{dt} &= -\frac{1}{R}(2.4k^2 + 2.4) - \frac{0.31k}{k^2 + 1}Ro b. \end{aligned} \quad (29)$$

Taking fourth order derivative, e.g., ∂_2^4 , ∂_3^4 , lends the solution near the domain boundaries to significant numerical errors. To avoid such errors, all integrations will be limited to wall-normal regions outside the viscous sublayer. In arriving at (29), we have also neglected terms that are significantly smaller than the retained ones.

The presence of multiple states requires (29) to have two or more non-trivial nodes, which in turn requires the following cubic equation of k^2 have two physically viable roots:

$$(k^2 + 1)^2(k^2 + 14/7.8) - Ck^2 = 0. \quad (30)$$

Figure 14 shows the bifurcation diagram, which leads to the same conclusions.

D Shell model

The shell model of energy cascades in an isotropic turbulent flow reads

$$\left(\frac{d}{dt} + \nu k_n^2\right) u_n = i(k_n u_{n+2}^* u_{n+1}^* - b k_{n-1} u_{n+1}^* u_{n-1}^* - c k_{n-2} u_{n-1}^* u_{n-2}^*) + f_n. \quad (31)$$

It models the time evolution of a velocity fluctuation $u_n(t)$ over a wavelength $k_n = k_0 \lambda^n$, with λ , the intershell ratio, usually set to 2. The nonlinear coupling conserves the energy with $b = 1/2$ and $c = -(1 - b)$. A equilibrium condition is obtained by forcing the flow at the large scale, i.e., $f_n = \delta_{1n}$. Despite its simple form, shell model yields flow statistics that are nearly identical to those from an isotropic turbulent flow. Further details of the shell model could be found in the review by Biferale (2003). The trajectory in figure 5 (b) is a plot in the phase space of $|u_2|$ and $|u_4|$. For our calculation, the number of shells is $N = 21$, the wavenumber of the first shell is $k_1 = 0.05$,

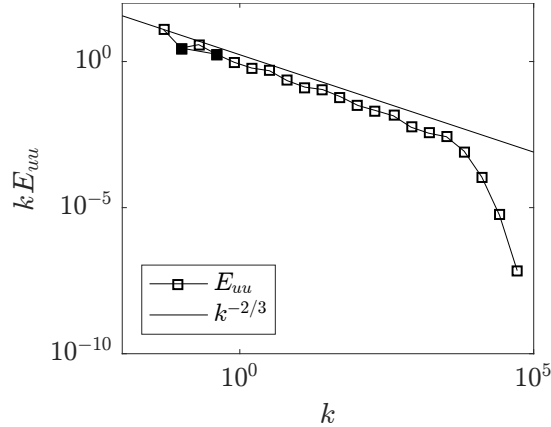


Figure 15: Premultiplied shell model energy spectrum. The 2nd and the 4th modes, whose trajectory is plotted in figure 5, are colored black.

the molecular viscosity is $\nu = 5e - 6$, and the forcing term is $f_1 = 0.1(1 + 1j)$. Figure 15 shows the premultiplied shell model energy spectrum, kE_{uu} . We see that kE_{uu} follows $k^{-2/3}$ closely.

References

- G. Ahlers, D. Funfschilling, and E. Bodenschatz. Heat transport in turbulent rayleigh-bénard convection for $\text{Pr} \approx 0.8$ and $\text{Ra} \lesssim 10^{15}$. In *Journal of Physics: Conference Series*, volume 318, page 082001. IOP Publishing, 2011.
- W. Anderson. Non-periodic phase-space trajectories of roughness-driven secondary flows in high-Re boundary layers and channels. *J. Fluid Mech.*, 869:27–84, 2019.
- L. Biferale. Shell models of energy cascade in turbulence. *Ann. Rev. Fluid Mech.*, 35(1):441–468, 2003.
- P. G. Drazin and W. H. Reid. *Hydrodynamic stability*. Cambridge University Press, 2004.
- B. F. Farrell and P. J. Ioannou. Structure and spacing of jets in barotropic turbulence. *Journal of the atmospheric sciences*, 64(10):3652–3665, 2007.
- B. F. Farrell and P. J. Ioannou. Statistical state dynamics: a new perspective on turbulence in shear flow., 2014.
- B. F. Farrell, D. F. Gayme, and P. J. Ioannou. A statistical state dynamics approach to wall turbulence. *PHILOS T R SOC A*, 375(2089):20160081, 2017.
- U. Frisch. *Turbulence: the legacy of AN Kolmogorov*. Cambridge university press, 1995.
- B. Galanti and A. Tsinober. Is turbulence ergodic? *Physics Letters A*, 330(3-4):173–180, 2004.
- M. Gul, G. E. Elsinga, and J. Westerweel. Experimental investigation of torque hysteresis behaviour of Taylor–Couette flow. *J. Fluid Mech.*, 836:635–648, 2018.
- Y. Huang, Z. Xia, M. Wan, Y. Shi, and S. Chen. Hysteresis behavior in spanwise rotating plane couette flow with varying rotation rates. *Phys. Rev. Fluids*, 4(5):052401, 2019.
- S. G. Huisman, R. C. Van Der Veen, C. Sun, and D. Lohse. Multiple states in highly turbulent taylor–couette flow. *Nature communications*, 5(1):1–5, 2014.
- A. J. Majda and I. Timofeyev. Remarkable statistical behavior for truncated Burgers–Hopf dynamics. *Proc Natl Acad Sci*, 97(23):12413–12417, 2000.

- I. Marusic, J. P. Monty, M. Hultmark, and A. J. Smits. On the logarithmic region in wall turbulence. *J. Fluid Mech.*, 716, 2013.
- M.-L. Rapún and J. M. Vega. Reduced order models based on local POD plus Galerkin projection. *J Comput Phys*, 229(8):3046–3063, 2010.
- F. Ravelet, L. Marié, A. Chiffaudel, and F. Daviaud. Multistability and memory effect in a highly turbulent flow: Experimental evidence for a global bifurcation. *Phys. Rev. Lett.*, 93(16):164501, 2004.
- F. Ravelet, A. Chiffaudel, and F. Daviaud. Supercritical transition to turbulence in an inertially driven von kármán closed flow. *J. Fluid Mech.*, 601:339–364, 2008.
- R. Stevens, J. Zhong, H. Clercx, G. Ahlers, and D. Lohse. Transitions between turbulent states in rotating Rayleigh–Bénard Convection. *Phys. Rev. Lett.*, 103:024503, 2009.
- K. Taira, S. L. Brunton, S. T. Dawson, C. W. Rowley, T. Colonius, B. J. McKeon, O. T. Schmidt, S. Gordeyev, V. Theofilis, and L. S. Ukeiley. Modal analysis of fluid flows: An overview. *AIAA Journal*, pages 4013–4041, 2017.
- A. Tsinober. *An informal introduction to turbulence*, volume 63. Springer Science & Business Media, 2001.
- E. van der Poel, R. Stevens, and D. Lohse. Connecting flow structures and heat flux in turbulent Rayleigh–Bénard convection. *Phys. Rev. E*, 84:045303, 2011.
- R. C. van der Veen, S. G. Huisman, O.-Y. Dung, H. L. Tang, C. Sun, D. Lohse, et al. Exploring the phase space of multiple states in highly turbulent taylor-couette flow. *Phys. Rev. Fluids*, 1(2):024401, 2016.
- Q. Wang, Z. Wan, R. Yan, and D. Sun. Multiple states and heat transfer in two-dimensional tilted convection with large aspect ratios. *Phys. Rev. Fluids*, 3:113503, 2018.
- P. Wei, S. Weiss, and G. Ahlers. Multiple transitions in rotating turbulent Rayleigh–Bénard Convection. *Phys. Rev. Lett.*, 114:114506, 2015.
- S. Weiss and G. Ahlers. Effect of tilting on turbulent convection: cylindrical samples with aspect ratio $\gamma = 0.50$. *J. Fluid Mech.*, 715:314–334, 2013.
- S. Weiss, R. Stevens, J. Zhong, H. Clercx, D. Lohse, and G. Ahlers. Finite-size effects lead to supercritical bifurcations in turbulent rotating Rayleigh–Bénard Convection. *Phys. Rev. Lett.*, 105:224501, 2010.
- H.-D. Xi and K.-Q. Xia. Flow mode transitions in turbulent thermal convection. *Phys. Fluids*, 20(5):055104, 2008.
- Z. Xia, Y. Shi, Q. Cai, M. Wan, and S. Chen. Multiple states in turbulent plane couette flow with spanwise rotation. *J. Fluid Mech.*, 837:477–490, 2018.
- Z. Xia, Y. Shi, M. Wan, C. Sun, Q. Cai, and S. Chen. Role of the large-scale structures in spanwise rotating plane couette flow with multiple states. *Phys. Rev. Fluids*, 4:104606, 2019.
- Y.-C. Xie, G.-Y. Ding, and K. Xia. Flow topology transition via global bifurcation in thermally driven turbulence. *Phys. Rev. Lett.*, 120:214501, 2018.
- X. I. A. Yang, Z. H. Xia, J. Lee, Y. Lv, and Y. J. Mean flow scaling in a spanwise rotating channel. *Phys. Rev. Fluids*, 2020a. doi: Inpress.
- Y. Yang, W. Chen, R. Verzicco, and D. Lohse. Multiple states and transport properties of double-diffusive convection turbulence. *Proc. Nat. Acad. Sci.*, 2020b. doi: 10.1073/pnas.2005669117.

- N. Yokoyama and M. Takaoka. Hysteretic transitions between quasi-two-dimensional flow and three-dimensional flow in forced rotating turbulence. *Phys. Rev. Fluids*, 2:092602(R), 2017.
- D. S. Zimmerman, S. A. Triana, and D. P. Lathrop. Bi-stability in turbulent, rotating spherical couette flow. *Phys. Fluids*, 23(6):065104, 2011.